Title: **Mesoscopic-scale functional networks in the primate amygdala**

Authors: Jeremiah K Morrow[1,2], Michael X Cohen[3,4], *Katalin M Gothard[1]

Affiliations:
(1) Department of Physiology, University of Arizona, Tucson, AZ 85716
(2) Department of Behavioral Neuroscience, Oregon Health and Sciences University, Portland, OR 97126
(3) Radboud University Medical Center, Nijmegen, Netherlands
(4) Donders Center for Neuroscience, Nijmegen, Netherlands

Corresponding Author:
Katalin M. Gothard, 1501 N. Campbell Ave. Rm# 4103, Tucson, AZ 85716.
kgothard@email.arizona.edu

OVERVIEW:

Number of pages: 42
Number of figures 4 (+ 2 supplementary)
Number of Tables: 0

Structure and word count
Abstract: 150
Introduction: 585
Results: 1226
Conclusions: 878
Intro, results, conclusions: 2689
Methods: 3019
References: 46 (+4 methods specific references)

Conflict of interest: The authors declare no competing finamical interests.

Author Contributions: JKM: experimental design, data collection, data analysis, manuscript preparation, MXC: data analysis, manuscript preparation, KMG: experimental design, manuscript preparation

1

Abstract:

The primate amygdala performs multiple functions that may be related to the anatomical heterogeneity of its nuclei. At the level of single neurons, each function is reflected in stimulus- and task-specific responses. Given that neurons with a particular response profile are not clustered in any of the nuclei, single units may be too fine-grained to shed light on the mesoscale organization of the amygdala. We have extracted from local field potentials recorded simultaneously from multiple locations within the primate amygdala (*Macaca mulatta*) spatially defined and statistically separable responses to visual, tactile, and auditory stimuli. A generalized eigendecomposition-based method of source separation isolated coactivity patterns, or components, that in neurophysiological terms correspond to putative subnetworks. Some component spatial patterns mapped onto the anatomical organization of the amygdala, while other components reflected integration across nuclei. These components differentiated between visual, tactile, and auditory stimuli suggesting the presence of functionally distinct parallel subnetworks.

Introduction

The division of the amygdala into nuclei reflects the developmental origins and the input-output connections of each nucleus with other structures (Amaral et al. 1992; Swanson and Petrovich 1998; Pessoa et al. 2019). Cell-type specific circuit dissection of the rodent amygdala revealed further compartmentalization of the amygdala (reviewed by Duvarci and Pare 2014; Janak and Tye 2015; Gafford and Ressler 2016; Fadok et al. 2018). The anatomical compartmentalization is rarely reflected in the response properties of single neurons (e.g., Beyeler et al., 2018; Kyriazi et al., 2018; Jeremiah Morrow et al., 2019; Putnam & Gothard, 2019). This is not surprising given the difficulty in capturing the activity of functional networks by subsampling the constituent neurons, especially when the network includes neurons with diverse response properties. Indeed, the neuron is no longer considered the physiological unit that explains functional states in the brain (Buzsáki 2010; Yuste 2015). At the other end of the spectrum of scale, neuroimaging techniques that monitor the activity of brain-wide networks cannot reliably capture nuclear or subnuclear activation in the amygdala. The local field potentials (LFPs), reflecting the aggregate activity of hundreds to tens of thousands of neurons (Buzsáki, Anastassiou, and Koch 2012; Einevoll et al. 2013; Pesaran et al. 2018), may provide a more adequate mesoscopic-scale view of intra-amygdala activity. Although task-relevant LFP signals have been successfully extracted from the amygdala of non-primate species in the context of fear conditioning (Paré 2002; Seidenbecher et al. 2003; Courtin et al. 2014; Stujenske et al. 2014), anticipatory anxiety (Paré 2002), and reward learning (Popescu, Popa, and Paré 2009), remarkably little is known about the information content of the local field potentials in the primate amygdala.

We recently reported that the majority of multisensory neurons in the monkey amygdala not only respond to visual, tactile, and auditory stimuli but also discriminate, via different spike train metrics, between sensory modalities and even between individual stimuli of the same sensory modality (Morrow,

Mosher, and Gothard 2019). Multisensory neurons and neurons selective for a particular sensory modality were not clustered in any nucleus or subnuclear region, suggesting an organization scheme in spatially distributed but functionally coordinated networks. We expected that the combined excitatory, inhibitory, and neuromodulatory effects elicited by different sensory modalities would be better captured in the dynamics of the LFPs than by the response properties of single neurons (Mazzoni et al. 2008; Buzsáki, Anastassiou, and Koch 2012). Specifically, we explored the hypothesis that stimuli of different sensory modalities elicit different spatiotemporal patterns of activity in the local field potentials recorded from linear arrays of electrodes. Rather than analyze the signals on each contact independently, we used a method of non-orthogonal covariance matrix decomposition called generalized eigendecomposition (GED) to identify co-activity patterns across the set of contacts. Because neural sources project linearly and simultaneously to multiple contacts, linear multivariate decomposition methods are highly successful at separating functionally distinct but spatially overlapping sources (Parra et al. 2005). These co-activity patterns (also called 'components') are the product of putative functional networks within the brain. GED has been shown to reliably reconstruct network-level LFP dynamics in both simulated and empirical data that are often missed by conventional methods of source-separation (De Cheveigné and Parra 2014; Van Veen et al. 1997; Cohen 2017; Parra et al. 2005) Here, we adapted this method to our data and discovered multiple, statistically dissociable patterns of network activity tied to the functional and spatial structure of the amygdala that was missed by the analysis of single-unit activity (Morrow, Mosher, and Gothard 2019).

Results

We monitored LFPs simultaneously from the entire dorso-ventral expanse of the amygdala with linear electrode arrays (V-probes, Plexon Inc., Dallas, TX) that have 16 equidistant contacts (400 µm spacing, Figure 1). We systematically sampled the medio-lateral and anterior-posterior regions of the amygdala during different recording sessions. In each session the signals were referenced to the common

average across the 16 contacts; this ensured that our signals were locally generated and not volume conducted from distant, e.g., cortical regions. Sets of eight visual, tactile and auditory stimuli were presented to the monkey as static images, gentle airflow, and random sounds (Figure 1). Each stimulus was presented 12-20 times and was followed by juice reward. All stimuli were specifically chosen to be unfamiliar and devoid of any inherent or learned significance to the animal. Stimuli with socially salient content like faces or vocalizations were avoided, as were images or sounds associated with food (e.g., pictures of fruit or the sound of the feed bin opening). Airflow nozzles were never directed toward the eyes or into the ears to avoid potentially aversive stimulation of these sensitive areas.

The LFP signal was compared between a baseline window (from -1.5 to -0.5 s relative stimulus onset) and a stimulus window (from 0 to +1.0 s relative to stimulus onset). Ninety-five percent of the contacts showed significant changes in LFP activity relative to baseline (623/656, 95.0% of all contacts, Wilcoxon rank-sum tests; Bonferroni corrected for 16 comparisons, $\alpha = 0.01/16 = 0.000625$). Rather than analyze the signals on each contact individually, we used a guided source-separation method, called generalized eigendecomposition (GED), to identify covariation patterns across the contacts that were maximally activated during stimulus delivery relative to the baseline period (Figure 2a-c). We then assessed whether these covariation patterns, also called 'components,' were spatially defined and modality-specific (Figure 2b-g) (for further details see Methods). Note that unlike principal components analysis, GED components do not have an orthogonality constraint, which facilitates physiologically interpretability (Cohen 2017).
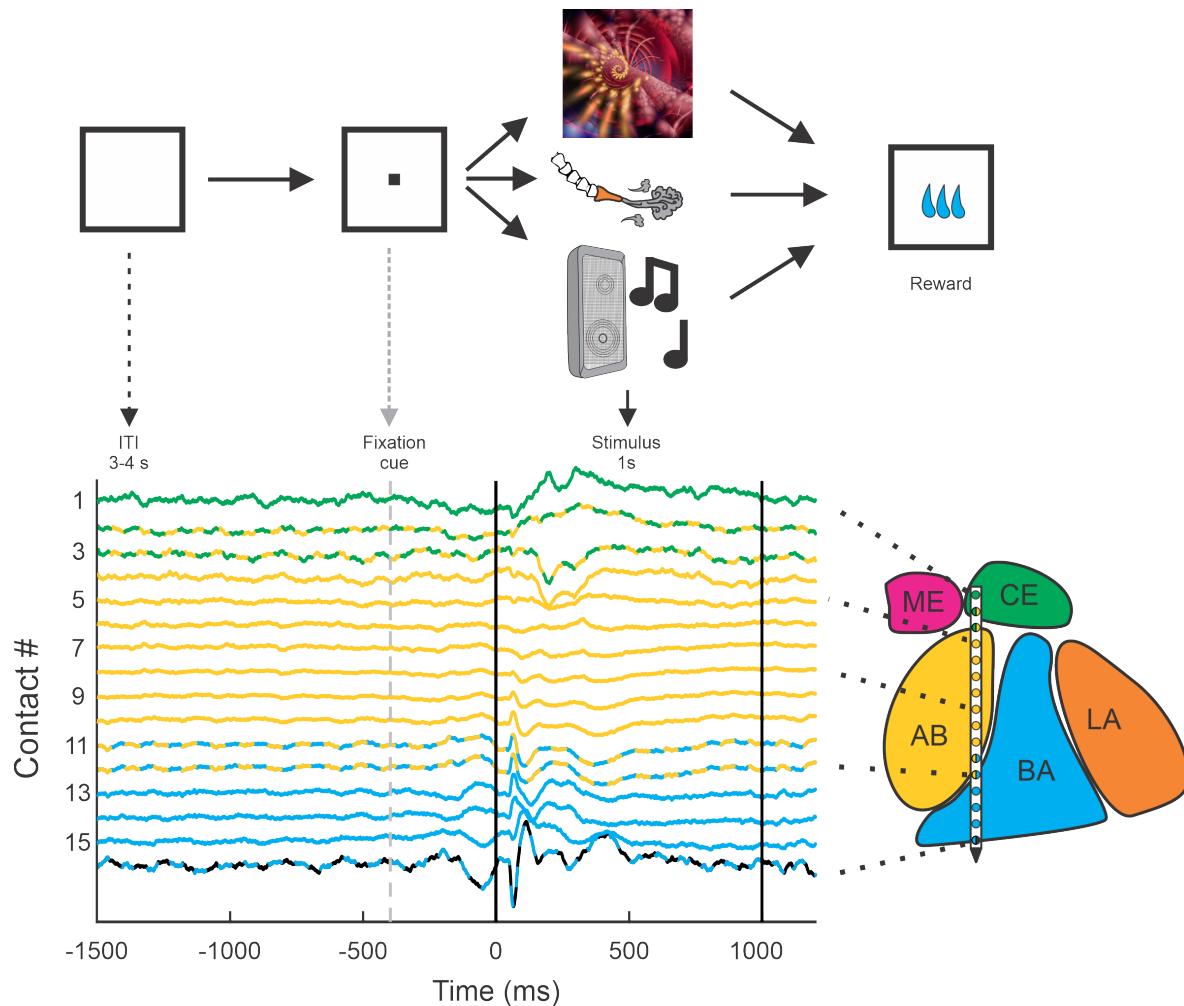
5

Figure 1. Behavioral setup and example average traces across all trials on each of the 16 contacts.

All trials were separated by a 3-4 second inter-trial interval (ITI) and preceded by a visual fixation cue presented at the center of a monitor in front of the animal. If the monkey successfully fixated on the cue, a single stimulus from one of the three sensory modalities (visual, tactile, auditory) was presented. All trials were followed by a brief delay (0.7-1.4 s) before a small consistent amount of juice was delivered. The color code of the peri-event LFP activity corresponds to the estimated location of the recording electrode within the nuclei of the amygdala. The lines with alternating colors refer to contacts located within 200 μm of an anatomical boundary between nuclei. ME = medial, magenta; CE = central, green; AB = accessory basal, yellow; BA = basal, cyan; LA = lateral, orange; non-amygdala contacts are colored black.

6

We found that between 1 and 5 components were simultaneously active during each recording session (figure 2h-i), leading to a total of 116 statistically significant components obtained from 41 sessions (significance was computed via permutation testing with corrections for multiple comparisons; see Methods). Removing contacts estimated to be outside of the amygdala from the analysis eliminated 24 components, emphasizing the importance of the spatial location of each contact (Figure 2 j-k). Only results from significant components are discussed for the remainder of this manuscript (see Methods for the criterion of significance).

The relative contribution of the signal from each contact to a particular component can be visualized in a 'component map' (figure 2d and 2f). This map can then be co-registered with the anatomical map of the amygdala to reveal whether contacts in different nuclei contribute to the components in distinct ways. Each component also has its own time series (figure 2e and 2g) that results from passing the raw LFP signals though the associated eigenvector to obtain a reconstructed signal that corresponds to the estimated output of the subnetwork captured in the component (Haufe et al. 2014).
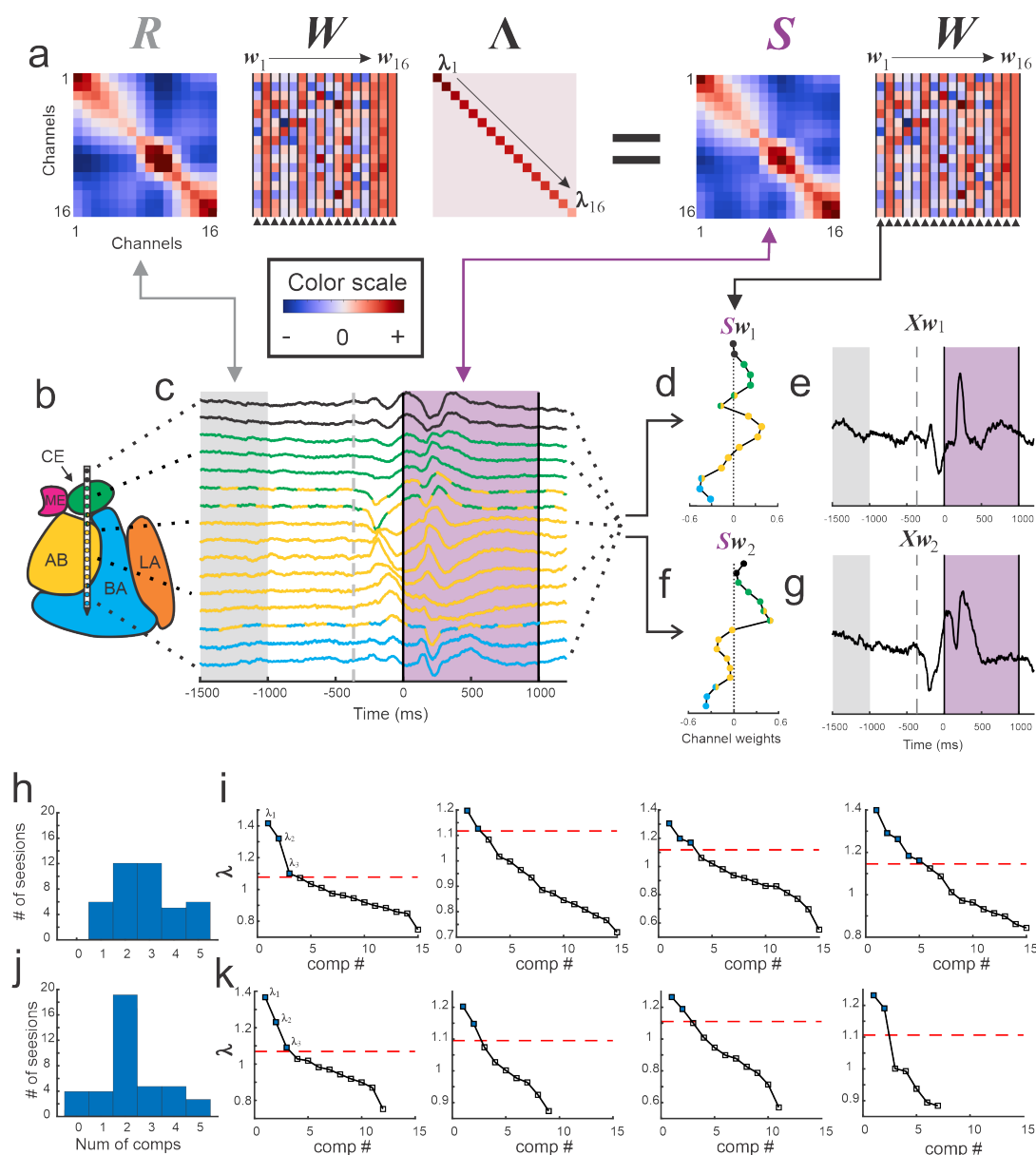
Figure 2. Visualization of GED.

(a) The elements of the equation for generalized eigendecomposition (RW = SWΛ), where R and S are 16x16 covariance matrices (corresponding to the 16 contacts) derived from baseline and stimulus activity respectively. These contact covariance matrices were generated for each trial and then averaged over trials (see Methods). The columns in the W matrix (highlighted by the arrowheads below the plot) contain the eigenvectors. Each eigenvector from the matrix can be written as w_n (indicated by the $w_1 \rightarrow w_{16}$ above the plots). The diagonal matrix of eigenvalues is represented by Λ. The individual eigenvalues are denoted by $\lambda_1 \rightarrow \lambda_{16}$ shown along the diagonal. A general color scale for the heatmap images is shown under the left side of the equation. (b) MRI-based reconstruction of recording sites in this session. (c) The average

8

*peri-stimulus LFP for each contact (color convention is the same as in Figure 1). Light gray shading indicates the baseline period and the purple shading denotes the stimulus delivery. The time of fixspot onset is shown as the gray dotted line. Note that the data in **c** are contained in a time-by-contacts matrix (represented by **X** in subsequent equations). **(d)** Example of the component map associated with the largest eigenvalue (created by multiplying the stimulus covariance matrix with an eigenvector, **Sw₁**). **(e)** The component time series associated with this eigenvalue. This time series is created by multiplying the LFP data matrix (i.e., **X**) with the eigenvector (**Xw₁**). **(f, g)** the same as for **d** and **e** but associated with the second largest eigenvalue. **(h)** Histogram of the number of significant components per session when including all contacts regardless of location (i.e., within or outside of the amygdala). **(i)** Scree plots of the eigenvalues derived from GED from four example sessions when all contacts were included in analysis regardless of location. In the scree plots, the points above the dotted line correspond to the significant eigenvalues. **(j)** Histogram of the number of significant components per session when only amygdala contacts were included in the analysis. **(k)** Scree plots of the eigenvalues from the same sessions in **i** but only using amygdala contacts. Note that decreasing the number of contacts decreases the number of total components that GED is able to extract. This does not always result in decreases in the number of significant components (left two panels); however, small (right middle) and occasionally large (far right) decreases in the number of significant components were observed.*

GED components map onto anatomical boundaries

The component maps show the extent to which the signals recorded from each anatomically localized contact in the amygdala contribute to the putative subnetwork captured by the component (Figure 3). The farther a contact weight value is from 0, the more the signal on that particular contact contributes to the component or subnetwork. Adjacent contacts that fall on one side of the zero line co-vary, and thus contribute similarly to the same component. Values of opposing signs (positive vs negative) make opposing contributions to the components (i.e., signals on contacts associated with positive weights inversely covary with the signals on contacts associated with negative weights). We applied a change-point detection algorithm (Lavielle 2005; Killick, Fearnhead, and Eckley 2012) to cluster the contacts

according to shifts in the rolling average of adjacent values in the component maps (see Methods). The boundaries of the statistical clusters matched both internal and external anatomical boundaries of the amygdala (Figure 3), which were estimated through a combination of high-resolution MRI and histology (Figure S1).

This is important because GED is a statistical decomposition method with no information about the anatomical location of the contacts from which the signals were collected. Moreover, this method discovered subnuclear divisions that neuroimaging would not be able to detect but are well known from histological analyses. For example, in Figure 3e and 3f the horizontal dotted lines intersecting the basal nucleus correspond to known boundaries between the magnocellular, intermediate, and parvocellular subdivisions (Amaral et al. 1992).

We quantified the match between the statistical grouping of contacts and the anatomical grouping of contacts as a percent overlap (see Methods). The overall number of matching contacts was 723/1072 (67.4%). We then determined which of the components (first, second, etc., see histogram in Fig 2h-j) showed the largest match between the statistical grouping and the anatomical grouping of contacts. Only the first components showed statistically better than chance overlap (249/349, 71.3%, paired t-test, $t = 2.76$, $df = 40$, $p = 0.009$, 1000 permutations, Bonferroni corrected for five comparisons, $\alpha = 0.05/5 = 0.01$).
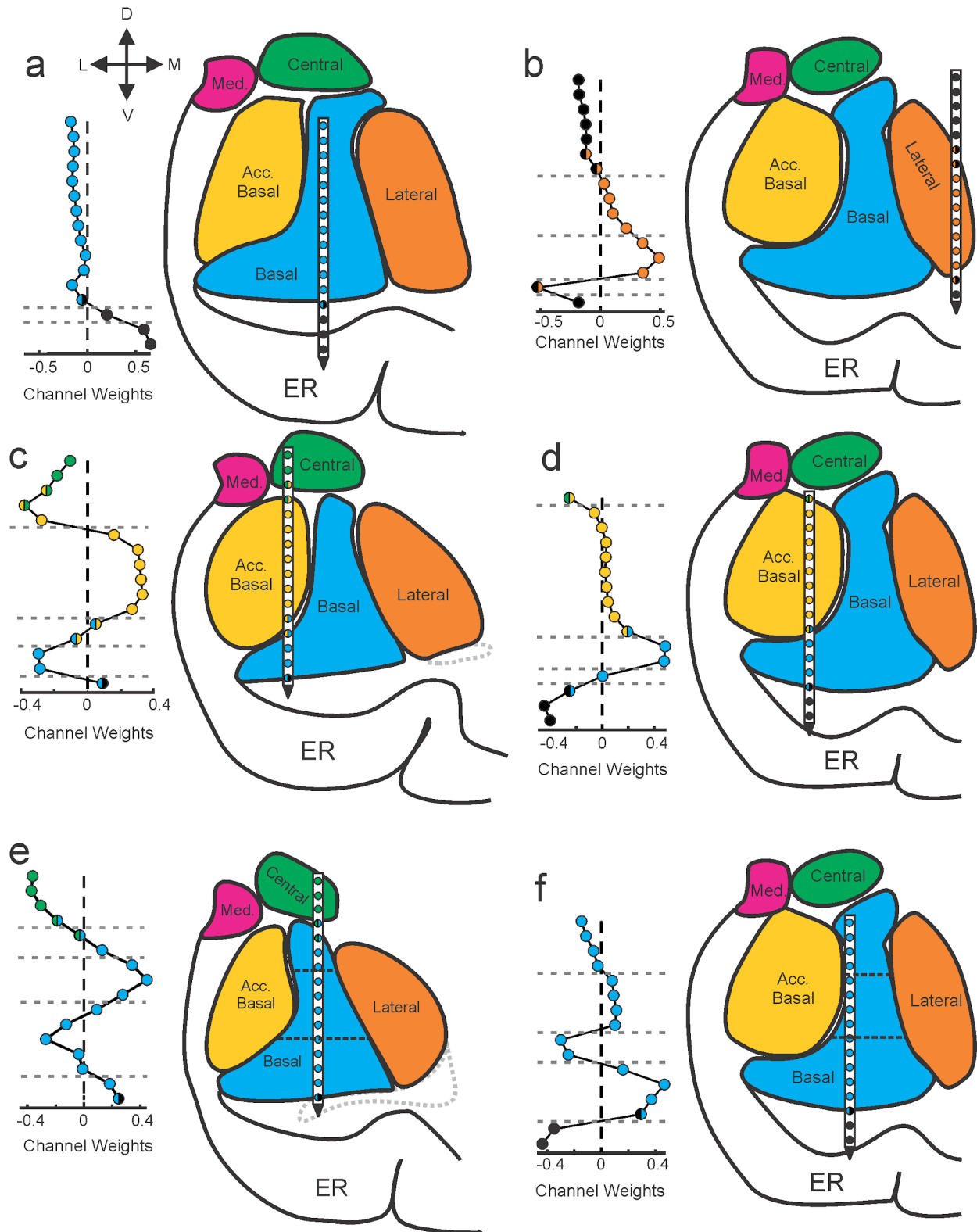
Figure 3. Components map onto anatomical boundaries.

*Six examples of how component maps (left) match the MRI-based reconstruction of the electrode array positions (right). On each component map the x axis corresponds to the weight calculated for each contact of the V-probe and the y axis lists the contacts. In each panel, the colors of the contact weights match their estimated nuclear locations following the same convention as in previous figures. Gray dotted lines in the component map plots denote change points in the contact weights that statistically separate groups of contacts based on their coactivity patterns (see Methods). Ventricles are contoured in light gray dotted lines. Med = medial nucleus; Acc. basal = accessory basal nucleus; ER = entorhinal cortex. **(a-b)** Examples of large transitions in contact weights at boundaries between the amygdala and surrounding tissue, particularly on the ventral contacts. **(c-d)** Examples of component maps in which the statistical clustering (dotted horizontal lines) match the geometry of the nuclear boundaries. **(e-f)** Two examples of component maps in which the statistical boundaries correspond to known subnuclear divisions of the basal nucleus.*

GED components discriminate between sensory modalities

It is possible that the selectivity for sensory modality seen at the single-unit level in the amygdala (Morrow, Mosher, and Gothard 2019) is also evident in the components obtained by GED. Time-frequency analyses of the component time series showed that each subnetwork responded selectively to visual, tactile, or auditory stimuli or a combination thereof (Figure 4). Of the 116 identified components, 102 discriminated between sensory modalities in at least one frequency range for at least one sensory modality (cluster-mass t-tests, $\alpha = 0.01$, see Methods), as shown by the change in power elicited by stimuli of each sensory modality (Figure 4 a-f). Only 13 out of 102 components showed responses restricted to a single sensory modality. These results replicate, at a larger spatial scale, our findings from the single unit analyses (Morrow, Mosher, and Gothard 2019). The power profiles of the component time series were modality-selective but not modality specific, i.e., the processing of visual, tactile, or auditory stimuli was not restricted to a particular frequency domain or a particular latency relative to stimulus onset. Sensory

12

modalities were better differentiated at lower frequencies (Wilcoxon rank-sum tests, $\alpha = 0.01$; Figure 4g). Typically, the largest changes in low-frequency power (<10 Hz) were elicited by visual stimuli, followed by tactile stimuli, with the lowest values for auditory stimuli (Figure 4g). The same observation holds when only assessing components with multisensory responses (72/89 components), (cluster-mass t-tests, $\alpha = 0.01$; figure 4h-j); visual stimuli elicited larger power changes than tactile, which in turn elicited larger changes than auditory stimuli.

We created a spectral profile based on the significant component signals across all datasets (figure 4k). The spectra show prominent peaks around the delta (3.5-4.5 Hz), theta (6-8), low-gamma (~38 Hz) and high-gamma (63-75 Hz) frequency bands. When we eliminated the contribution of contacts located outside the amygdala to the spectra shown in figure 4k, the overall shape and location of the peaks remained similar (Figure 4l). The similarities between these two spectra suggest that the components reported here indeed reflect neural activity within the amygdala and not inherited from adjacent structures (further support for the components emerging from contacts within the amygdala is provided by Figure S2).
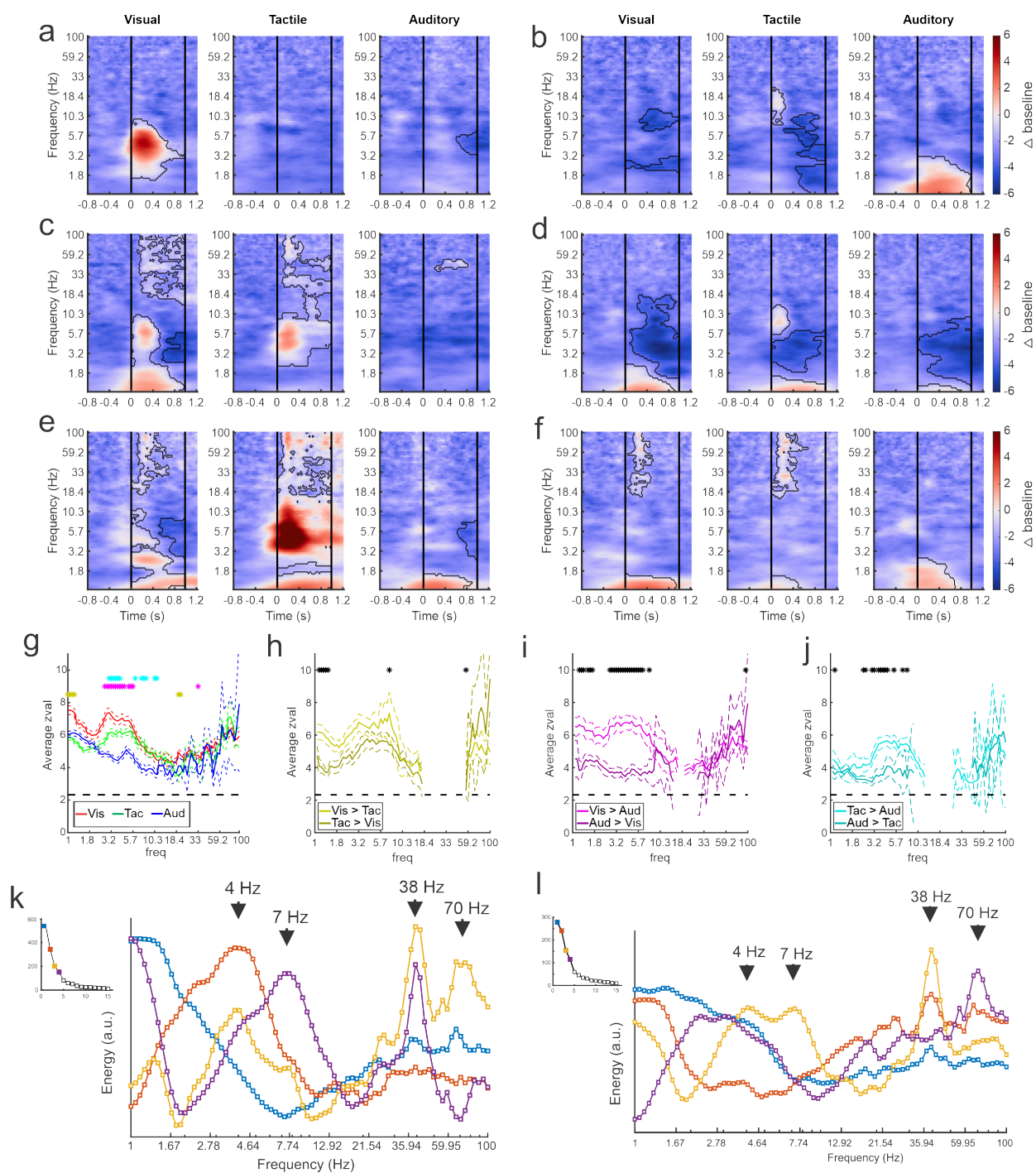
13

Figure 4: GED-based components show modality-selective but not modality-specific changes in multiple frequency bands

*(**a-f**) Example time-frequency plots created from the GED-based components separated by stimulus modality (i.e., visual, tactile, and auditory). Each time-frequency plot shows the relative difference in power between the baseline and stimulus periods for a GED-based component time series (scale at far*

14

*right, 1-100 Hz, logarithmic scale). Black contoured lines denote clusters of significant changes in power between baseline and stimulus delivery (see Methods). Solid lines at 0 and 1s denote the start and end of stimulus delivery. (**a**) Increase in power centered around 4.5 Hz elicited by visual stimuli. (**b**) Increase in power across low (1-3 Hz) frequencies elicited by auditory stimuli with minor power changes for visual and tactile stimuli. (**c**) Moderate increase in power from 1-2 and 5-8 Hz for visual stimuli and 4-8 Hz for tactile stimuli. (**d**) Moderate decreases in power for all stimuli center around 4 Hz. (**e**) Disparate responses to visual, tactile, and auditory stimuli. Note how multiple frequencies bands show time varying increases in power for all three stimuli, however, the time-frequency power around 1 Hz is similar between the sensory modalities. (**f**) A component with fairly similar responses across sensory modalities but note the lack of high frequency activity for auditory stimuli. (**g**) Maximum separation of the selectivity for sensory modality occurs below 10 Hz. Solid lines represent the mean z-value within significant clusters at each frequency for each modality (visual = red, tactile = green, auditory = blue). Dotted lines denote mean +/- 5 standard errors of the mean. Gold asterisks denote significant differences in cluster-mass values between the visual and tactile responses, magenta asterisks denote significant differences between visual and auditory, and cyan asterisks denote differences between visual and auditory. (**h-j**) Pairwise comparisons of selectivity between modalities for components that responded to multiple sensory modalities. Solid lines represent mean and dotted lines represent the mean +/- 5 standard errors of mean. (**k**) Spectral profiles were generated from the significant components from all sessions. PCA was then used to extract the prominent features of these profiles (right) and corresponding scree plots (left) (see Methods). These plots were created using all available data regardless of estimated location of the contact. The spectral profile and scree plots were color coded according to the rank of the associated component (1st = blue; 2nd = orange; 3rd = yellow; 4th = purple). The power at each frequency is plotted in arbitrary units of energy. (**l**) Same as in **k** but only using data from contacts that were estimated to be within the amygdala.*

Conclusions

Neither the fine grain single unit literature nor the coarser neuroimaging literature brought conclusive evidence for or against the functional compartmentalization of the primate amygdala. Only a small fraction of the single unit studies reported an uneven distribution of neurons with particular response properties across the nuclei (e.g., Clayton P Mosher, Zimmerman, and Gothard 2010; Zhang et al. 2013;

Grabenhorst et al. 2019). To complicate things further, an increasing number of single unit studies reported that neurons in the amygdala respond to multiple stimulus dimensions and task parameters (Saez et al. 2015; Kyriazi, Headley, and Pare 2018b; Munuera, Rigotti, and Salzman 2018; Morrow, Mosher, and Gothard 2019; Putnam and Gothard 2019). These multidimensional neurons are not clustered in any nuclei or subnuclear region, which seems to be at odds with the compartmentalized view of the amygdala. This contradiction may be resolved by considering large ensembles of neurons, instead of single neurons, as the as the organizational unit of the amygdala (for a critique of the neuron-based concepts see Yuste, 2015).

Remarkably little is known about the neurophysiology of the primate amygdala at the network level, due in part to its layerless architecture that is not expected to generate the predictable LFP patterns observed in layered structures like the neocortex or the hippocampus. In the primate amygdala, each nucleus and nuclear subregion has different cytoarchitecture and also distinct input-output connections with both cortical and subcortical structures (Ghashghaei and Barbas 2002; Sah et al. 2003; Amaral et al. 1992). For example, projections from the amygdala to dopamingeric neurons in the substantia nigra mainly arise from the central nucleus. These central nucleus projections are further distinguished into medial and lateral subdivisions that terminate in separate subregions of the substantia nigra (Fudge and Haber 2000). Likewise, the subregions of the dorsolateral prefrontal cortex are reciprocally connected to distinct nuclear subdivisions of the basolateral complex (Amaral and Price 1984). This organization could give rise to parallel, nucleus-anchored processing loops that induce nuclear-specific patterns of neural activity. It is also possible that the rich intra-amygdala connectivity (Pitkänen and Amaral 1991; Bonda 2000) distributes signals arriving to or originating from a particular area of the amygdala across multiple nuclei, evening out functional differences expected based on structural consideration alone.

Here, we provide evidence for a mesoscopic organization of the amygdala, into putative

16

subnetworks of neurons identified by guided source separation of the local field potentials recorded from multicontact electrodes. The presence of *any* identifiable network demonstrates that a layered architecture is not a prerequisite for meaningful organization of LFP activity. The presence of *multiple* subnetworks suggests functional compartmentalization. Importantly, the strongest of the subnetworks were contoured by the internal and external boundaries of the nuclei of the amygdala. This is remarkable because the GED is "blind" to the spatial arrangement of the contacts on the V-probe and to the location of the V-probe in the amygdala. This is evidence that a mesoscale physiological feature of the amygdala (the LFP), unlike the single units, is bound by anatomical constraints. The implications of this finding are twofold: (1) expanding GED to three-dimensions (using multiple linear electrode arrays at different medio-lateral and rostral-caudal positions) will likely generate a more complete functional map of the primate amygdala, and (2) these new physiological features revealed by GED can then be set in register with the known neuroanatomy encompassing all nuclei.

The subnetworks identified by GED are functionally relevant because the coactivity patterns elicited by visual, tactile, and auditory stimuli discriminated between sensory modalities (as shown in in Figure 4). While no activity pattern was specific for a particular sensory modality, the majority of activity patterns carried information about one or multiple sensory modalities. For example, the activity of the subnetwork shown in Figure 4e conveys information about all sensory modalities albeit with different power in each frequency band, without any one frequency band being assigned to a single sensory modality. This complements the selectivity and specificity pattern of the single unit responses recorded simultaneously from the same contacts (Morrow, Mosher, and Gothard 2019).

Further progress is expected from expanding the network analyses presented here to cover field-field or spike-field interactions between the amygdala and connected structures. The first few attempts in this direction have been successful in revealing the directionality of interactions between the amygdala

17

and the anterior cingulate cortex during aversive learning (Taub et al. 2018). Brain-wide circuits are indeed the domain where LFP analyses might be most revealing (Pesaran et al. 2018). Indeed, brain states, like affect or attention, can be characterized by spatiotemporal interactions between a hub and the cortical areas functionally linked to the hub. For example, the pulvinar and amygdala are hubs placed at the intersection of multiple brain-wide circuits and they both are expected to coordinate the activity of multiple cortical and subcortical areas during behavior (Bridge, Leopold, and Bourne 2016; Pessoa et al. 2019). The coordination of spatial attention across brain-wide network, has been recently attributed directional selective, theta-band interactions between the pulvinar, the frontal eye fields, and the parietal cortex (Fiebelkorn, Pinsk, and Kastner 2019). The multivariate signal decomposition techniques used here, expanded to datasets recorded simultaneously from multiple nodes of amygdala-centered circuits, has great potential to determine how the amygdala coordinates the activity of other structures during social and affective behaviors.

Materials and Methods

A. Surgical procedures

Two adult male rhesus macaques, F and B (weight 9 and 14 kg; age 9 and 8 years respectively), were prepared for neurophysiological recordings from the amygdala. The stereotaxic coordinates of the right amygdala in each animal were determined based on high-resolution 3T structural magnetic resonance imaging (MRI) scans (isotropic voxel size = 0.5 mm for monkey F and 0.55 mm for monkey B). A square (26x26 mm inner dimensions) polyether ether ketone (PEEK), MRI compatible recording chamber was surgically attached to the skull and a craniotomy was made within the chamber. The implant also included three titanium posts, used to attach the implant to a ring that was locked into a head fixation system. Between recording sessions, the craniotomy was sealed with a silicone elastomer that can prevent growth and scarring of the dura (Spitler and Gothard 2008). All procedures comply with the NIH guidelines for the use of non-human primates in research and have been approved by The University of Arizona's Institutional Animal Care and Use Committee.

B. Experimental Design

B1. Electrophysiological procedures

Local field potential activity was recorded with linear electrode arrays (V-probes, Plexon Inc., Dallas, TX) that have 16 equidistant contacts along a 236 μm diameter shaft. A single electrode array was acutely lowered into the right amygdala for each recording session using a Thomas Recording Motorized Electrode Manipulator (Thomas Recording GmbH, Giessen, Germany). The first contact of the array was located 300 μm from the tip of the probe and each subsequent contact was spaced 400 μm apart; this arrangement allowed us to monitor simultaneously the entire dorso-ventral expanse of the amygdala. Impedance for each contact typically ranged from 0.2 to 1.2 MΩ. The anatomical location of each electrode was calculated by drawing the chamber to scale on a series of coronal MR images and aligning

19

the chamber to fiducial markers (co-axial columns of high contrast material). Histological verification of these recording site estimates was done in monkey B (see supplemental Methods). During recordings, slip-fitting grids with 1 mm distance between cannula guide-holes were placed in the chamber, this allowed a systematic sampling of most medio-lateral and anterior-posterior locations in the amygdala. Twenty-three-gauge cannulae were inserted through the guide holes and placed 4-6 mm into the cortex. V-probes were driven through the cannula and down to the amygdala at a rate of 70-100 μm per second, slowing to 5-30 μm per second after the tip of the V-probe crossed into the estimated location of the central nucleus.

The analog signal from each channel on the V-probe was digitized at the headstage (Plexon Inc., HST/16D Gen2) before being sent through a Plexon pre-amplifier, filtering from 0.1 to 300 Hz and sampling continuously at 40 kHz. LFP was extracted from each contact and down sampled at 1 kHz for analysis. Signals were initially referenced to the shaft of the electrode and were re-referenced offline to the average signal across all electrodes on the probe (i.e., common average reference). This referencing scheme minimizes the contribution of volume conduction from distant sources that spread to all contacts simultaneously and ensured that the recorded LFPs reflected local mesoscale brain dynamics.

B2. Stimulus delivery

The monkey was seated in a primate chair and placed in a recording booth featuring a 1280x720 resolution monitor (ASUSTek Computer Inc., Beitou, Taiwan), two Audix PH5-VS powered speakers (Audix Corporation, Wilsonville, OR) to either side of the monitor, a custom made airflow delivery apparatus (Crist Instruments Company Inc., Damascus, MD), and a juice spout. Juice delivery was controlled by a peristaltic pump (New Era Pump Systems, Inc., Farmingdale, NY, model: NE-9000). The airflow system was designed to deliver gentle, non-aversive airflow stimuli to various locations on the

face and head (i.e., the pressure of the air flow was set to be perceptible but not aversive). The system, based on the designs of Huang & Sereno and Goldring *et al.* (Huang and Sereno 2007; Goldring et al. 2014) consists of a solenoid manifold and an airflow regulator (Crist Instruments Company, Inc.), which controlled the intensity of the airflow directed toward the monkey. Low pressure vinyl tubing lines (ID 1/8 inch) were attached to ten individual computer-controlled solenoid valves and fed through a series of Loc-line hoses (Lockwood Products Inc., Lake Oswego, OR). The Loc-line hoses were placed such that they did not move during stimulus delivery and were out of the monkey's line of sight. All airflow nozzles were placed ~2 cm from the monkeys' fur and outflow was regulated to 20 psi. At this pressure and distance, the air flow caused a visible deflection of the monkeys' fur.

Stimulus delivery was controlled using custom written code in Presentation Software (Neurobehavioral Systems, Inc., Berkeley, CA). The monkey's eye movements were tracked by an infrared eye tracker (ISCAN Inc., Burlington, MA, camera type: RK826PCI-01) with a sampling rate of 120 Hz. Eye position was calibrated prior to every session using a 5-point test. During the task the animal was required to fixate for 125-150 ms a central cue ("fixspot") that subtended 0.35 dva. Successful fixation was followed by the delivery of a stimulus randomly drawn from a pool of neutral visual, tactile, and auditory stimuli. In monkey F, there was no delay between the fixspot offset and stimulus onset, while in monkey B a 200 ms delay was used. Stimulus delivery lasted for 1 s and was followed (after a delay of 700-1200 ms) by juice reward. Each stimulus was presented 12-20 times and was followed by the same amount of juice (~1 mL). Trials were separated by a 3-4 s inter-trial interval (ITI).

For each recording session, a set of eight novel images were selected at random from a large pool of pictures of fractals and objects. Images were displayed centrally on the monitor and covered ~10.5x10.5 dva area. During trials with visual stimuli, the monkey was required to keep his eye within the boundary

21

of the image. If the monkey looked outside of the image boundary, the trial was terminated without reward and repeated following an ITI.

Tactile stimulation was delivered to eight sites on the face and head: the lower muzzle, upper muzzle, brow, and above the ears on both sides of the head (see Morrow, Mosher, and Gothard 2019 for further details). The face was chosen because in a previous study a large proportion of neurons in the amygdala respond to tactile stimulation of the face (Mosher et al. 2016). Two "sham" nozzles were directed away from the monkey on either side of the head to control for the noise made by the solenoid opening and/or by the movement of air through the nozzle. Pre-experiment checks ensured that the airflow was perceptible (caused visible deflection of hair) but not aversive. The monkeys displayed slight behavioral responses (e.g., minor startle responses) to the stimuli during the first habituation session, but they did not overtly respond to these stimuli during the experimental sessions.

For each recording session, a set of eight novel auditory stimuli were taken from freesound.org, edited to be 1 second in duration, and amplified to have the same maximal volume using Audacity sound editing software (Audacity® version 2.1.2, RRID: 007198). Sounds included musical notes from a variety of instruments, synthesized sounds, and real-world sounds (e.g., tearing paper). The auditory stimuli for each session were drawn at random from a stimulus pool using a MATLAB script (The MathWorks Inc., Natick, MA, version 2016b, RRID: SCR_001622).

All stimuli were specifically chosen to be unfamiliar and devoid of any inherent or learned significance for the animal. Stimuli with socially salient content like faces or vocalizations were avoided as were images or sounds associated with food (e.g., pictures of fruit or the sound of the feed bin opening). Airflow nozzles were never directed toward the eyes or into the ears to avoid potentially aversive stimulation of these sensitive areas.

C. Data Analysis

LFP signals were extracted for analysis in MATLAB using scripts from the Plexon MATLAB software development kit and down sampled to 1000 Hz in MATLAB. Artifacts (e.g., signals from broken contacts, sharp spikes in the LFP caused by movement of the animal, or 60 cycle line noise) were removed from the signal prior to further analyses.

C1. Peri-event LFP

The LFP signal from every trial was taken for each contact for two time windows: a baseline window from -1.5 to -0.5 s relative stimulus onset and a stimulus delivery window from 0 to +1.0 s relative to stimulus onset. The medians of these two distributions of values were compared using a Wilcoxon rank-sum test to determine the number of contacts with significant event-related changes in LFP signals. These tests were Bonferroni-corrected for multiple comparisons within each session (i.e., tests for differences on each of 16 contacts results in an adjusted alpha level of $0.01/16 = 0.000625$).

C2. Covariance matrices

Covariance matrices were generated by taking the LFP signal for each contact during a time window (baseline or stimulus delivery) to get a timepoints-by-contacts matrix for a given trial. The LFP at each timepoint on each trial was subtracted from the mean LFP across time on the trial. The timepoints-by-contacts matrix was then multiplied by its transpose to create a square, symmetric covariance matrix for a single trial (i.e., contacts-by-contacts covariance matrix). These trial-wise covariance matrices were generated for both the baseline and stimulus delivery time periods. The average of the stimulus covariance matrices made the S matrix and the average of the baseline matrices made the R matrix.

C3. Generalized eigendecomposition

Generalized eigendecomposition (GED) was used to generate components that maximized stimulus related changes in activity. GED is a *guided source-separation* technique based on decades of

23

statistics and engineering work (Tomé 2006; De Cheveigné and Parra 2014; Van Veen et al. 1997; Parra et al. 2005). Eigendecomposition can be used to decompose a multivariate signal to generate "components" that capture patterns of covariance across recording contacts. We use generalized eigendecomposition as an optimization algorithm to design a spatial filter (a set of weights across all contacts) that maximizes the ratio of the stimulus-related covariance matrix to the pre-stimulus covariance matrix (also called the baseline or reference matrix). This can be expressed through the Rayleigh quotient:

$$w_{max} = argmax \left\{ \frac{w^T S w}{w^T R w} \right\}$$

Where S is the covariance matrix generated from data collected during the stimulus delivery time window, R is a covariance matrix generated from the data collected during the baseline window, and w is an eigenvector (w^T is the transpose of w). When $w = w_{max}$, the value of the ratio is an eigenvalue, λ. The full solution to this equation is obtained from a generalized eigendecomposition ($RW = SW\Lambda$, Figure 2), where W is a matrix with eigenvectors in the columns, and Λ is a diagonal matrix containing the eigenvalues. Eigenvectors convey the directions of covariance patterns that maximally separate the S and R matrices (i.e., contact-by-contact contributions to the component) and eigenvalues relay the magnitude of the difference between S and R. The goal of this maximization function is therefore to find multichannel covariance patterns that are prominent during stimulus delivery but not during baseline. Should the co-activity patterns be similar during the baseline and stimulus windows, the ratio S/R will be close to one ($\lambda = 1$), however, large differences in multichannel activity that arise during stimulus delivery will manifest as relatively larger eigenvalues ($\lambda >> 1$).

To determine a statistical threshold for λ, we shuffled the labels for the S and R matrices for each trial and performed GED 500 times to create a null distribution of eigenvalues that are associated with activity that was not time-locked to stimulus onset. The observed eigenvalues were compared to this null

24

distribution and components associated with eigenvalues above the 99th percentile of this distribution were considered to be statistically significant (similar in concept to a 1-tailed t-test with an alpha level of 0.01).

C4. Component maps and time series

While eigenvectors are difficult to interpret on their own because they both boost signal and suppress noise (i.e., any irrelevant activity), multiplication of an eigenvector by a covariance matrix creates a forward model of the spatial filter that is easier to visually inspect (Haufe et al. 2014). We refer to these filters as "component maps" because they convey the relative contribution of each contact to a component signal (i.e., each element of the eigenvector is related to how the LFP on a specific contact contributed to the extracted component). For these data, component maps are generated by multiplying the stimulus covariance matrix, S, with the eigenvector corresponding to the nth component (Sw_n).

Component time series were created by multiplying the time-by-contacts LFP data matrix with an eigenvector. These time-series data are the weighted average of the activity across contacts that is captured by the component.

C5. Anatomical grouping versus statistical clustering of contacts

If there is an influence of the spatial location of contacts on component activity, this should manifest as abrupt shifts in sequential values in the component maps. If these shifts correlate with anatomically defined nuclear boundaries, this would suggest that the cytoarchitectural heterogeneity of the nuclei manifests as a potentially functional signal. To assess this possibility, we used the MATLAB function "*findchangepnts*" to identify transitions in the channel weight values. This function works to find the points at which sequential values deviate from some statistical parameter by exhaustively grouping values in all possible sequential configurations and determining the residual error given by a test statistic.

25

We set this function to detect an unspecified number of transitions in the mean values of sequential points ("*Statistic*" input set to mean with no specified minimum or maximum number of transitions). To prevent overfitting, a proportionality constant of 0.05 was used ("*MinThreshold*" input set to 0.05). The proportionality constant is a fixed penalty for adding subsequent changepoints such that new changepoints that do not reduce the residual error by at least 0.05 are rejected (see MATLAB documentation for further details on the findchangepnts function).

To determine if these statistically defined changepoints matched anatomical boundaries estimated via high-resolution MRI, we grouped all contacts on a recording session according to their estimated anatomical location. If all contacts located within a single nucleus were statistically grouped together (i.e., no within nucleus changepoint was detected), each contact was considered to be matching between the two grouping methods. If contacts from multiple nuclei were grouped together, each additional contact from a non-matching nucleus was not included from the total matching count. Likewise, when contacts were grouped anatomically but separated in the statistical clustering, only the grouping that captured the most contacts was counted as matching (e.g., if 7 contacts were grouped anatomically but this was split by changepoints into one group of four contacts and another of three contacts, only the four contact group was counted). Contacts estimated to be within 200 μm of a nuclear boundary were excluded from this assessment (i.e., not considered matching or non-matching) due to the slight uncertainty in their anatomical grouping. As we were only interested in the spatial information within the amygdala, non-amygdala contacts were also excluded from this analysis.

To determine if the percentage of matching contacts was statistically better than chance, we randomly paired changepoint maps with anatomical maps and calculated the matching percentage for all sessions (i.e., we shuffled the anatomical and statistical maps relative to one another). We repeated this 1000 times for each component to get a null distribution of "matching" values. We then compared the

observed distributions of matching values for each component group (1 to 5) to this null distribution using paired t-tests, Bonferroni corrected for the 5 comparisons ($\alpha = 0.05/5 = 0.01$). This allowed us to determine whether the statistical mapping of the average 1st to 5th component matched the anatomical mapping better than expected by chance.

C6. Time-frequency decompositions

Component time series were created by multiplying the LFP data with an eigenvector. Time frequency (TF) analysis on the component time series was implemented via convolution with a series of complex Morlet wavelets (logarithmically spaced from 1 to 100 Hz in 80 steps) following standard procedures (Cohen 2014). To determine whether any sections of the time-frequency power differed significantly from baseline we used a cluster-mass test similar in design to the method described in Maris and Oostenveld, 2007. TF power matrices were generated for a baseline time window from -1.5 s to -1.0 s relative to stimulus onset and a stimulus time window from 0 to +1.0 s relative to stimulus onset. The difference between these two matrices and was then taken to find how TF power changed from baseline to stimulus onset. We then repeated this process shuffling both the labels for the baseline and stimulus time windows and the exact start time of the windows (randomly within 500 ms of actual start time). This generated a set of difference maps that were not time-locked to any specific event during the trials. We repeated this 1000 times and used the mean and standard deviation from these shuffles to z-score normalize the values in the observed difference matrix. Each of the individual difference maps was z-scored using the same parameters as for the observed data. Lastly, clusters of values in these matrices in which the z-scores on adjacent positions were greater than 2.33 (corresponding to $\alpha = 0.01$) were created. The z-scores within these clusters were then summed to create a "cluster-mass value" for each cluster in the shuffled permutations and the actual data. The cluster-mass values from the difference matrix

27

generated from the observed value was compared to the distribution of maximum cluster-mass values generated by the shuffled permutations (i.e., we compared only the largest cluster in each shuffle to the observed data). Observed clusters-mass values greater than 99% of the values obtained via the shuffles were considered to be statistically significant and are outlined in black in the plots in figure 4 a-f.

C7. Spectral Profiles

Power spectra were created from each of the component time series. Principle components analysis was used to extract the prominent features of these spectral profiles across all components. The signals associated with the four principal components accounting for the most explained variance (figure 4i-j, scree plots) were extracted and plotted (figure 4i-j).

REFERENCES

Amaral, D. G., and J. L. Price. 1984. "Amygdalo-Cortical Projections in the Monkey (Macaca Fascicularis)." *The Journal of Comparative Neurology* 230 (4): 465–96. https://doi.org/10.1002/cne.902300402.

Amaral, David G, Joel L Price, Asla Pitkanen, and Thomas S Carmichael. 1992. "Anatomical Organization of the Primate Amygdaloid Complex." In *The Amygdala: Neurobiological Aspects of Emotion, Memory, and Mental Dysfunction*, Aggleton J, 1–66. New York: Wiley-Liss, INC.

Anna Beyeler, Authors, Chia-Jung Chang, Margaux Silvestre, Clé mentine Lé, Praneeth Namburi, Craig P Wildes, Kay M Tye, and Anna Beyeler. 2018. "Organization of Valence-Encoding and Projection-Defined Neurons in the Basolateral Amygdala Article Organization of Valence-Encoding and Projection-Defined Neurons in the Basolateral Amygdala." *Cell Reports* 22: 905–18. https://doi.org/10.1016/j.celrep.2017.12.097.

Bonda, Eva. 2000. "Organization of Connections of the Basal and Accessory Basal Nuclei in the Monkey Amygdala." *European Journal of Neuroscience* 12 (6): 1971–92. https://doi.org/10.1046/j.1460-9568.2000.00082.x.

Bridge, Holly, David A. Leopold, and James A. Bourne. 2016. "Adaptive Pulvinar Circuitry Supports Visual Cognition." *Trends in Cognitive Sciences*. Elsevier Ltd. https://doi.org/10.1016/j.tics.2015.10.003.

Buzsáki, György. 2010. "Neural Syntax: Cell Assemblies, Synapsembles, and Readers." *Neuron*. NIH Public Access. https://doi.org/10.1016/j.neuron.2010.09.023.

Buzsáki, György, Costas A Anastassiou, and Christof Koch. 2012. "The Origin of Extracellular Fields and Currents - EEG, ECoG, LFP and Spikes." *Nature Reviews Neuroscience* 13 (6): 407–20. https://doi.org/10.1038/nrn3241.

Cheveigné, Alain De, and Lucas C. Parra. 2014. "Joint Decorrelation, a Versatile Tool for Multichannel Data Analysis." *NeuroImage*. Academic Press Inc. https://doi.org/10.1016/j.neuroimage.2014.05.068.

Cohen, Michael X. 2014. *Analyzing Neural Time Series Data*. Cambridge, MA: MIT Press.

Cohen, Michael X. 2017. "Multivariate Cross-Frequency Coupling via Generalized Eigendecomposition," January, 26.

Courtin, J, N Karalis, C Gonzalez-Campo, H Wurtz, and C Herry. 2014. "Persistence of Amygdala Gamma Oscillations during Extinction Learning Predicts Spontaneous Fear Recovery." *Neurobiology of Learning and Memory*, Extinction, 113 (September): 82–89. https://doi.org/10.1016/j.nlm.2013.09.015.

Duvarci, Sevil, and Denis Pare. 2014. "AMYGDALA MICROCIRCUITS CONTROLLING LEARNED FEAR." *Neuron* 82 (5): 966–80. https://doi.org/10.1016/j.neuron.2014.04.042.

Einevoll, Gaute T, Christoph Kayser, Nikos K Logothetis, and Stefano Panzeri. 2013. "Modelling and Analysis of Local Field Potentials for Studying the Function of Cortical Circuits." *Nature Reviews Neuroscience* 14 (11): 770–85. https://doi.org/10.1038/nrn3599.

Fadok, Jonathan P., Milica Markovic, Philip Tovote, and Andreas Lüthi. 2018. "New Perspectives on Central Amygdala Function." *Current Opinion in Neurobiology*. Elsevier Ltd. https://doi.org/10.1016/j.conb.2018.02.009.

Fiebelkorn, Ian C., Mark A. Pinsk, and Sabine Kastner. 2019. "The Mediodorsal Pulvinar Coordinates the Macaque Fronto-Parietal Network during Rhythmic Spatial Attention." *Nature Communications* 10 (1). https://doi.org/10.1038/s41467-018-08151-4.

Fudge, J. L., and S. N. Haber. 2000. "The Central Nucleus of the Amygdala Projection to Dopamine Subpopulations in Primates." *Neuroscience* 97 (3): 479–94. https://doi.org/10.1016/S0306-

4522(00)00092-0.

Gafford, G. M., and K. J. Ressler. 2016. "Mouse Models of Fear-Related Disorders: Cell-Type-Specific Manipulations in Amygdala." *Neuroscience*. Elsevier Ltd. https://doi.org/10.1016/j.neuroscience.2015.06.019.

Ghashghaei, H T, and H Barbas. 2002. "Pathways for Emotion: Interactions of Prefrontal and Anterior Temporal Pathways in the Amygdala of the Rhesus Monkey." *Neuroscience* 115 (4): 1261–79. https://doi.org/10.1016/S0306-4522(02)00446-3.

Goldring, Adam B, Dylan F Cooke, Mary K L Baldwin, Gregg H Recanzone, Adam G Gordon, Tingrui Pan, Scott I Simon, and Leah Krubitzer. 2014. "Reversible Deactivation of Higher-Order Posterior Parietal Areas. {II}. Alterations in Response Properties of Neurons in Areas 1 and 2." *Journal of Neurophysiology* 112 (10): 2545–60. https://doi.org/10.1152/jn.00141.2014.

Grabenhorst, Fabian, Raymundo Báez-Mendoza, Wilfried Genest, Gustavo Deco, and Wolfram Schultz. 2019. "Primate Amygdala Neurons Simulate Decision Processes of Social Partners." *Cell* 177 (4): 986-998.e15. https://doi.org/10.1016/j.cell.2019.02.042.

Haufe, Stefan, Frank Meinecke, Kai Görgen, Sven Dähne, John-Dylan Haynes, Benjamin Blankertz, and Felix Bießmann. 2014. "On the Interpretation of Weight Vectors of Linear Models in Multivariate Neuroimaging." *NeuroImage* 87 (February): 96–110. https://doi.org/10.1016/j.neuroimage.2013.10.067.

Huang, Ruey-Song, and Martin I Sereno. 2007. "Dodecapus: An MR-Compatible System for Somatosensory Stimulation." *NeuroImage* 34 (3): 1060–73. https://doi.org/10.1016/j.neuroimage.2006.10.024.

Janak, Patricia H, and Kay M Tye. 2015. "From Circuits to Behaviour in the Amygdala." *Nature* 517 (7534): 284–92. https://doi.org/10.1038/nature14188.

31

Killick, R, P Fearnhead, and I A Eckley. 2012. "Optimal Detection of Changepoints with a Linear Computational Cost." *Journal of the American Statistical Association* 107 (500): 1590–98. https://doi.org/10.1080/01621459.2012.737745.

Kyriazi, Pinelopi, Drew B. Headley, and Denis Pare. 2018. "Multi-Dimensional Coding by Basolateral Amygdala Neurons." *Neuron* 99 (6): 1315-1328.e5. https://doi.org/10.1016/j.neuron.2018.07.036.

Lavielle, Marc. 2005. "Using Penalized Contrasts for the Change-Point Problem." *Signal Processing* 85 (8): 1501–10. https://doi.org/10.1016/j.sigpro.2005.01.012.

Maris, Eric, and Robert Oostenveld. 2007. "Nonparametric Statistical Testing of EEG- and MEG-Data." *Journal of Neuroscience Methods* 164 (1): 177–90. https://doi.org/10.1016/j.jneumeth.2007.03.024.

Mazzoni, Alberto, Stefano Panzeri, Nikos K. Logothetis, and Nicolas Brunel. 2008. "Encoding of Naturalistic Stimuli by Local Field Potential Spectra in Networks of Excitatory and Inhibitory Neurons." *PLoS Computational Biology* 4 (12): e1000239. https://doi.org/10.1371/journal.pcbi.1000239.

Morrow, J., C. Mosher, and K. Gothard. 2019. "Multisensory Neurons in the Primate Amygdala." *Journal of Neuroscience* 39 (19). https://doi.org/10.1523/JNEUROSCI.2903-18.2019.

Mosher, C P, P E Zimmerman, A J Fuglevand, and K M Gothard. 2016. "Tactile Stimulation of the Face and the Production of Facial Expressions Activate Neurons in the Primate Amygdala." *ENeuro* 3 (5). https://doi.org/10.1523/ENEURO.0182-16.2016.

Mosher, Clayton P, Prisca E Zimmerman, and Katalin M Gothard. 2010. "Response Characteristics of Basolateral and Centromedial Neurons in the Primate Amygdala." *The Journal of Neuroscience : The Official Journal of the Society for Neuroscience* 30 (48): 16197–207. https://doi.org/10.1523/JNEUROSCI.3225-10.2010.

Munuera, Jérôme, Mattia Rigotti, and C Daniel Salzman. 2018. "Shared Neural Coding for Social

Hierarchy and Reward Value in Primate Amygdala." *Nature Neuroscience* 21 (3): 415–23. https://doi.org/10.1038/s41593-018-0082-8.

Paré, D. 2002. "Amygdala Oscillations and the Consolidation of Emotional Memories." *Trends in Cognitive Sciences* 6 (7): 306–14. https://doi.org/10.1016/S1364-6613(02)01924-1.

Parra, Lucas C, Clay D Spence, Adam D Gerson, and Paul Sajda. 2005. "Recipes for the Linear Analysis of EEG." *NeuroImage* 28 (2): 326–41. https://doi.org/10.1016/j.neuroimage.2005.05.032.

Pesaran, Bijan, Martin Vinck, Gaute T Einevoll, Anton Sirota, Pascal Fries, Markus Siegel, Wilson Truccolo, Charles E Schroeder, and Ramesh Srinivasan. 2018. "Investigating Large-Scale Brain Dynamics Using Field Potential Recordings: Analysis and Interpretation." *Nature Neuroscience* 21 (7): 903–19. https://doi.org/10.1038/s41593-018-0171-8.

Pessoa, Luiz, Loreta Medina, Patrick R Hof, and Ester Desfilis. 2019. "Neural Architecture of the Vertebrate Brain: Implications for the Interaction between Emotion and Cognition." *Neuroscience & Biobehavioral Reviews* 107 (December): 296–312. https://doi.org/10.1016/j.neubiorev.2019.09.021.

Pitkänen, A, and D G Amaral. 1991. "Demonstration of Projections from the Lateral Nucleus to the Basal Nucleus of the Amygdala: A PHA-L Study in the Monkey." *Experimental Brain Research* 83 (3): 465–70. https://doi.org/10.1007/BF00229822.

Popescu, Andrei T, Daniela Popa, and Denis Paré. 2009. "Coherent Gamma Oscillations Couple the Amygdala and Striatum during Learning." *Nature Neuroscience* 12 (6): 801–7. https://doi.org/10.1038/nn.2305.

Putnam, Philip T., and Katalin M. Gothard. 2019. "Multidimensional Neural Selectivity in the Primate Amygdala." *ENeuro* 6 (5): ENEURO.0153--19.2019. https://doi.org/10.1523/ENEURO.0153-19.2019.

Saez, A, M Rigotti, S Ostojic, S Fusi, and C D Salzman. 2015. "Abstract Context Representations in Primate Amygdala and Prefrontal Cortex." *Neuron* 87 (4): 869–81. https://doi.org/10.1016/j.neuron.2015.07.024.

Sah, P, E S L Faber, M Lopez De Armentia, and J Power. 2003. "The Amygdaloid Complex: Anatomy and Physiology." *Physiological Reviews* 83 (3): 803–34. https://doi.org/10.1152/physrev.00002.2003.

Seidenbecher, Thomas, T Rao Laxmi, Oliver Stork, and Hans-Christian Pape. 2003. "Amygdalar and Hippocampal Theta Rhythm Synchronization During Fear Memory Retrieval." *Science* 301 (5634): 846–50. https://doi.org/10.1126/science.1085818.

Spitler, Kevin M, and Katalin M Gothard. 2008. "A Removable Silicone Elastomer Seal Reduces Granulation Tissue Growth and Maintains the Sterility of Recording Chambers for Primate Neurophysiology." *Journal of Neuroscience Methods* 169 (1): 23–26. https://doi.org/10.1016/j.jneumeth.2007.11.026.

Stujenske, Joseph M, Ekaterina Likhtik, Mihir A Topiwala, and Joshua A Gordon. 2014. "Fear and Safety Engage Competing Patterns of Theta-Gamma Coupling in the Basolateral Amygdala." *Neuron* 83 (4): 919–33. https://doi.org/10.1016/j.neuron.2014.07.026.

Swanson, Larry W, and Gorica D Petrovich. 1998. "What Is the Amygdala?" *Trends in Neurosciences* 21 (8): 323–31. https://doi.org/10.1016/S0166-2236(98)01265-X.

Taub, Aryeh Hai, Rita Perets, Eilat Kahana, and Rony Paz. 2018. "Oscillations Synchronize Amygdala-to-Prefrontal Primate Circuits during Aversive Learning." *Neuron* 97 (2): 291-298.e3. https://doi.org/10.1016/j.neuron.2017.11.042.

Tomé, Ana Maria. 2006. "The Generalized Eigendecomposition Approach to the Blind Source Separation Problem." *Digital Signal Processing* 16 (3): 288–302.

https://doi.org/10.1016/j.dsp.2005.06.002.

Veen, Barry D. Van, Wim Van Drongelen, Moshe Yuchtman, and Akifumi Suzuki. 1997. "Localization of Brain Electrical Activity via Linearly Constrained Minimum Variance Spatial Filtering." *IEEE Transactions on Biomedical Engineering* 44 (9): 867–80. https://doi.org/10.1109/10.623056.

Yuste, Rafael. 2015. "From the Neuron Doctrine to Neural Networks." *Nature Reviews Neuroscience*. Nature Publishing Group. https://doi.org/10.1038/nrn3962.

Zhang, Wujie, David M. Schneider, Marina A. Belova, Sara E. Morrison, Joseph J. Paton, and C. Daniel Salzman. 2013. "Functional Circuits and Anatomical Distribution of Response Properties in the Primate Amygdala." *Journal of Neuroscience* 33 (2): 722–33. https://doi.org/10.1523/JNEUROSCI.2970-12.2013.

SUPPLEMENTAL INFORMATION
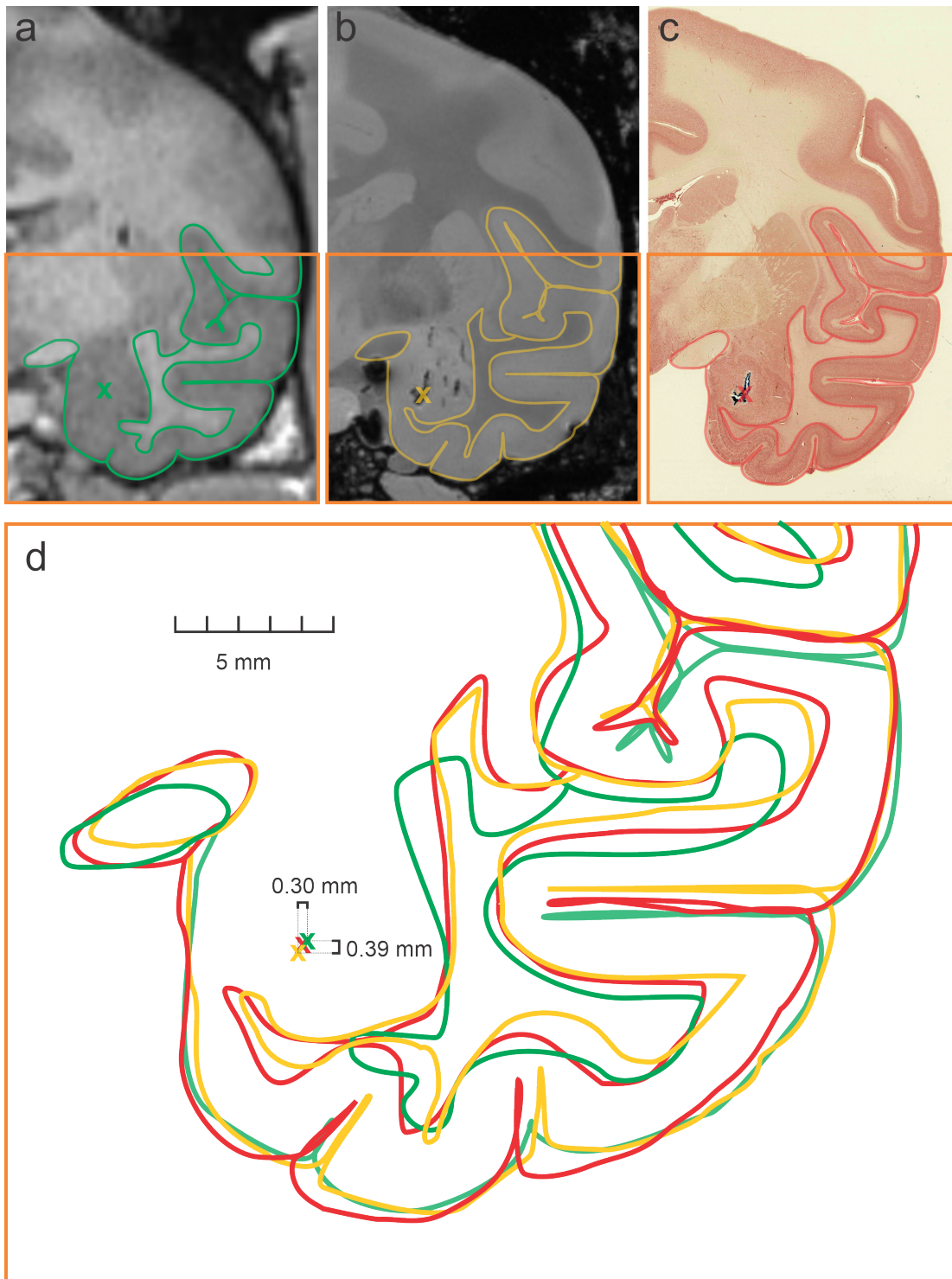
Supplemental Figure 1: Histological verification of electrode placement.

Coronal slices of the right hemisphere of the brain of monkey B at the anterior-posterior location of a dye injection into the amygdala (indicated by the X's in each image). **(a)** *3T MRI scan taken after the surgical implant of the recording chamber. The green X indicates the predicted site of a cell stain injected immediately preceding euthanasia and perfusion (4% PFA) of the brain. The targeting of the injection site and the estimated locations of the contacts were both calculated relative to the same stereotaxic coordinates used for initial implantation of the recording chamber.* **(b)** *An ex vivo, high-resolution 7T MRI. The scan was performed on the brain of monkey B ten weeks after perfusion and provided a more detailed visualization of the injection prior to histological processing. The gold X indicates the position of the dye injection. Note that electrode tracks can be seen dorsal and lateral to the injection site.* **(c)** *Histological verification of injection site estimates on a neutral-red stain. The red X indicates the position of the dye injection.* **(d)** *The estimated locations of the dye injection site along with the boundaries of major temporal lobe structures (contained in the orange boxes in* **a-c***) from the three images were overlaid. The numbers around the injection site reconstructions (i.e., the X's) indicate the distances between the centers of the farthest separated sites (green and gold) in the dorsal-ventral (0.39 mm) and medial-lateral (0.30 mm) axes. These distances show that even when taking the largest differences estimated injection location, the dorso-lateral and ventral-medial error is less than the space between two contacts on the V-probe. These results verify that reconstructions of contact positions should be accurate to within less than ~400 μm.*
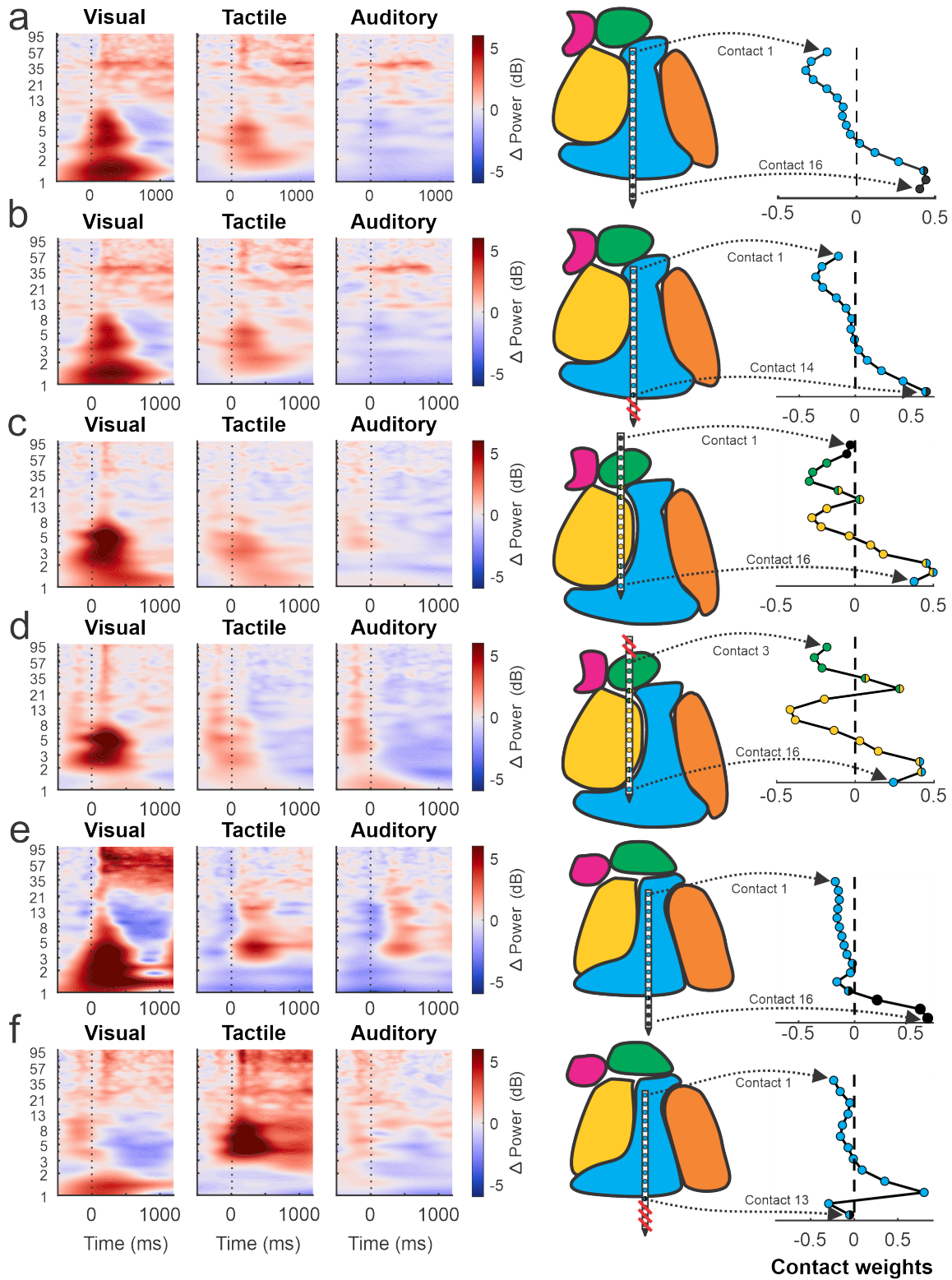
Supplemental figure 2. Effects of removing non-amygdala contacts on time-frequency decompositions

*The time-frequency plots (left) follow the same convention as in Figure 4, the MRI-based reconstructions (middle) follow the same convention as in Figure 1, and the spatial filter plots (right) follow the same convention as in figure 2. **(a)** A component generated from a recording where the two most ventral contacts were located outside of the amygdala (the two black contacts at the bottom of the plots). **(b)** Removal of these contacts has very little impact on the time-frequency activity of the component. Likewise, the component map maintains a similar structure, suggesting that much of the co-activity pattern captured by the component remained intact. **(c)** Here we show a time-frequency plot for a recording session where the two dorsal contacts outside the central nucleus of the amygdala. **(d)** When removing these contacts from analysis, some changes in the TF power was seen. For example, some of the increase in low frequency power elicited by visual stimuli was lost and more broad band increases in power immediately preceding the stimulus (i.e., the time of fixation on the pre-stimulus cue) are seen. The component map again remains largely unchanged. **(e)** Here several ventral contacts were estimated to be located below the amygdala (with the bottom contacts estimated to be in or near the entorhinal cortex). The component signal is heavily influenced by these ventral contacts (spatial filter, right). The time-frequency plots show large increases in power at low and high frequencies with a decrease in power in the beta range during delivery of visual stimuli. More moderate increases in power in the low to mid frequency ranges are observed for the tactile and auditory stimuli. **(f)** Removal of these contacts from analysis results in very different time-frequency plots. Much of the changes in power for the visual and auditory stimuli are lost; however, a large increase in power around the theta range (~4-8 Hz) and in the gamma bands (40-100 Hz) are now seen for the delivery of tactile stimuli. Unlike the previous two examples, the component map also shifted strongly with a large increase in the weight on contacts 11 and 12. When removing non-amygdala contacts, the majority of components remained (92/116, Figure 2h and 2j), albeit with some*

39

*changes as shown in **a-d**. Those that were eliminated were likely similar to what is shown in **e-f**, that is,*

components which were heavily driven by the signals on those non-amygdala contacts.

Supplemental Methods

MRI-based estimation of recording sites

In order to verify the accuracy of our recording system, we used a combination of high-resolution MRI and histology. Initial, *in vivo* 3T MRI scans were performed as described in the main Methods section to guide placement of the V-probe on each recording session. After all data collection from monkey B had finished, we selected a site in the center of the amygdala as the target of an injection of a cell staining dye (Blue Tissue Marking Dye^{TM}, Triangle Biomedical Sciences, Inc., Durham, NC) to determine the accuracy of estimates of the electrode positions (Figure S1a).

Injection procedure

The same methods described for guiding the placement of the electrode arrays during electrophysiological recordings were used to guide the insertion of a 30-gauge cannula into the amygdala of monkey B. A piece of metal tubing (outer diameter 640 µm) was attached near the top of the injection cannula using Gorilla Glue (Maine Wood Concept Inc., Cincinnati, OH) so that the cannula could be placed into the Motorized Electrode Manipulator in the same way as the V-probes. The cannula was thin enough to fit through the same guide tubes used to deliver the V-probes and was lowered at the same rate into the amygdala. A Hamilton syringe, attached to thin rubber tubing, was used to deliver 2 µl of dye over the course of 12 minutes to ensure ample staining of the target area. We allowed the cannula to sit for 30 minutes post injection before removing it from the amygdala. Approximately two hours following dye injection, the animal was prepped for euthanasia, perfused with 4% PFA, and decapitated. The head was placed in 4% PFA for two weeks.

7T ex vivo MRI

Fifteen days after euthanasia, the head was scanned using a 7T MRI scan with 250 μm isotropic voxels. Scan parameters were as follows: 86 mm ID quad volume coil; 3D gradient-echo with 250 μm isotropic resolution and matrix size of 320 x 288 x 256; TR = 100 ms; TE = 6 ms; FA = 30; and NA = 6.

Assessment of accuracy using MRIs and histology

Estimates of the location of the injection site were made independently for each of the three images (3T, 7T, and histology). The images from the 3T, 7T, and histology were then co-registered using major anatomical landmarks. The distances between all injection site estimates were measured and the largest difference in these values was used to ensure the most conservative assessment of the accuracy.